Comparison between average-atom and detailed-configuration-type calculations of the photoionization cross section of hot and dense aluminum plasmas

David Salzmann,* R. Y. Yin, and R. H. Pratt
Department of Physics and Astronomy, University of Pittsburgh, Pittsburgh, Pennsylvania 15260
(Received 4 September 1984; revised manuscript received 24 June 1985)

Photoionization cross sections in hot and dense aluminum plasmas have been obtained within the framework of a detailed-configuration (DC) model and two versions of the average-atom (AA) model: In the first the same non—local thermodynamic equilibrium (non-LTE) population distribution was used as that for the DC one (non-LTE-AA), whereas in the second an atom with LTE occupation numbers was used [Thomas-Fermi type (TF)-AA]. Even using the same non-LTE occupation numbers, significant differences were found in the photoionization cross sections as calculated by means of the non-LTE-AA and the DC models particularly near the edge regions. These differences include mainly the relative shift of the edges and their splitting which leads to a larger tip-to-dip ratio near the edge in the AA than that in the DC model, as well as a structured edge region in the DC model relative to the simple sharp edge in the AA model. Far from the edges in the high-photon-energy region, there are only minor differences in the predictions of the two models. The comparison between the non-LTE-AA and the TF-AA models reveals huge quantitative differences in low-density plasmas where a coronal equilibrium prevails; these originate from the different occupation numbers used in the two models. Such differences become smaller in a high-density plasma where the non-LTE-AA model has, practically, an LTE population similar to that of the TF-AA model.

I. INTRODUCTION

The effort concentrated in recent years on the research into hot and dense plasmas, particularly astrophysical and laser-produced plasmas, has stimulated extensive theoretical and experimental investigation of x-ray production and reabsorption in these plasmas. Two aspects of the x-ray production and/or reabsorption problem are of particular importance: first, x-ray absorption and reemission is a central process in the local energy balance of hot and dense plasmas; second, x-ray spectroscopy has special importance as a major diagnostic tool of dense plasmas, particularly in laser-produced plasmas where x-ray emission is the main detectable process carrying information on the plasma evolution during the stage of heating. From the emerging x-ray spectrum important information about the electron temperature, ion density, and the ionization state distribution can be unfolded. However, since the x-ray spectrum undergoes reabsorption inside the plasma, a good calculation of the absorption coefficient is required to obtain a unique interpretation of the experimental results. Similar problems were recently identified in astrophysical plasmas.[1]

A full computation of the photoabsorption coefficients meets the difficulty that a large number of photoionization cross sections are required, for all ionization stages, ground states, and excited states of the relevant ions in the plasma. This requires major computational effort, especially for high-Z materials. To overcome this problem an average-atom (AA) approximation is generally used,[2,3] which replaces the charge and excited-state distributions in a plasma by a single fictitious ionic species which has the average charge of the ions in the plasma and the average population distribution of the ions among the various excited states. Generally, this results in fractional occupation numbers. The atomic properties of this average atom are calculated in various schemes, of which the most popular is the Thomas-Fermi (TF) type of approximation,[2,4] which basically assumes a local thermodynamic equilibrium (LTE) in the plasma. Recently, Cauble, Blaha, and Davis[5] carried out a comparison of the photoionization cross section as calculated by three other approximations, namely, the density-functional theory[6] (DFT), the hypernetted-chain approximation (HNC), and the Debye-Hückel (DH) theory.

In recent years only a few attempts were made to carry out detailed-configuration-type (DC) calculations. A computation of the photoabsorption cross section of an aluminum plasma in the density range of 10^{20}—10^{22} cm^{-3} and temperature range of 32—1000 eV was carried out by Salzmann and Wendin.[7] In their calculation a non-LTE population distribution was used and a frozen-core Hartree-Fock (HF) method was used to calculate photoionization cross sections. The bound and free electrons were not, however, treated self-consistently, limiting the validity of their results to relatively "low" densities, below 10^{22} cm^{-3}. Recently, a few other DC-type calculations were reported which treat the bound and free electrons self-consistently. These include a paper by Skupsky,[8] who concentrated on the calculation of the level and line shifts in hot and dense neon plasmas. Blaha and Davis[9] solved the Schrödinger equation for a single hydrogenic neon ion immersed in a fully ionized hydrogen plasma, and calculated the variation with density of the level and line shifts as well as the Einstein coefficients and the collision strengths.

The transit time of a 1-keV photoelectron through the atom is of the order of 10^{-18} sec. If the characteristic time of the various atomic processes is much longer than this period, a well-defined atomic configuration can be assumed for the ionizing atom during the photoionization process. Under these circumstances the DC model is the appropriate physical picture to describe the process. In the other extreme, the atomic environment is likely to change repeatedly during the photoelectron-emission time and a statistical AA model for the atom would probably better describe the process. In all the examples of the present paper the characteristic time of the atomic processes ($\sim 10^{-13}$ sec) is very much longer than the photoelectron-emission time except very close to the threshold (electron energy $\ll 1$ eV), and one would expect that the DC model will be the more accurate one.

The AA model is a highly successful model which is used to calculate various thermodynamic parameters of high-density plasmas,[10] besides the photoionization cross sections, which could not be tackled by other computational means. However, in spite of its successes, the validity of the basic assumptions of the AA model was never justified by comparison with more accurate DC-type computations. It is the aim of the present paper to compare these two major models and to investigate the validity of the two basic assumptions of the AA model, namely, (i) how accurate is the photoionization cross section from an average-atom species versus the average of the cross sections from a realistic charge distribution which is represented by this average atom and (ii) how much inaccuracy is introduced into the AA model by the use of the LTE population distributions in density domains where LTE is known to be inadequate.

A high-temperature pure-aluminum plasma was chosen to illustrate our studies. Calculations were done at a constant temperature of $kT=500$ eV and ion densities n_T between 1×10^{20}–3×10^{23} cm^{-3} corresponding to plasma coupling constant[11] Γ between 0.3 and 4.5 ($\Gamma=\bar{Z}^2e^2/kTR$, where R is the ion-sphere radius) covering a range of transition from weakly to rather strongly coupled plasmas. In this density and temperature range the plasma consists mainly of hydrogenlike and heliumlike ions with a small percentage of fully ionized and lithiumlike species. Our choice of constant temperature was influenced by the fact that temperature variations cause, as a central effect, corresponding variations in the charge-state distributions and have only minor influence on the shifts of the eigenvalues or distortion of the wave functions, which are at the focus of the present paper. Nevertheless, some results of computations carried out by varying the temperature are presented in Sec. III. We made computations of the photoionization cross section, both in the DC and the AA frameworks, and compared results from the two models. In Sec. II our basic model is described, and the results are presented and analyzed in Sec. III.

II. THE BASIC FORMALISM

We consider an ion having nuclear charge Z and ionic charge Z_f positioned at $r=0$. The number of the bound electrons ($Z_b=Z-Z_f$) as well as their distribution among the various excited states are predetermined conditions of the problem to be solved. The ion together with Z_f free electrons are confined to the ion sphere $r\le R=(3/4\pi n_T)^{1/3}$. Beyond this sphere the distribution of the positive charge is assumed to neutralize exactly the negative electron distribution, thereby producing an electrically neutral background. Similar models, generally called ion-sphere models (ISM), were used in the literature,[10–12] sometimes with minor variations.

In our model both the bound and the free electrons are treated self-consistently in a central potential $V(r)$. More accurately, assuming some initial estimate for the free- and bound-electron charge distributions, the potential is obtained from the Poisson equation,

$$\nabla^2V(r)=-4\pi[n_f(r)+n_b(r)]\ , \tag{1}$$

where $n_f(r)$ and $n_b(r)$ are the free- and bound-electron densities, respectively. The bound-electron eigenvalues and wave functions are then obtained by solving the relativistic Dirac equation in this central potential $V(r)$,

$$[-i\boldsymbol{\alpha}\cdot\nabla+\beta mc^2+V(r)]\Psi_{\kappa m}=E\Psi_{\kappa m}\ , \tag{2}$$

where $\boldsymbol{\alpha}$ and β are the Dirac matrices, E is the total (including rest mass) energy of the bound electron, and

$$\Psi_{\kappa m}=\frac{1}{r}\begin{bmatrix} g_\kappa\Omega_{\kappa m} \\ if_\kappa\Omega_{-\kappa m}\end{bmatrix} \tag{3}$$

is the eigenfunction with the corresponding quantum numbers $\kappa=j\pm\frac{1}{2}$ and m. The radial functions $g_\kappa(r)$ and $f_\kappa(r)$ are the large and small components connected by the differential equations

$$\begin{aligned}\frac{dg_\kappa}{dr}&=[E+mc^2-V(r)]f_\kappa(r)-\frac{\kappa}{r}g_\kappa(r)\ ,\\ \frac{df_\kappa}{dr}&=\frac{\kappa}{r}f_\kappa(r)-[E-mc^2-V(r)]g_\kappa(r)\ ,\end{aligned} \tag{4}$$

and $\Omega_{\kappa m}$ stands for the angular components of the wave function. From these wave functions the bound-electron spatial distribution can be calculated as

$$n_b(r)=\sum_\kappa(2j+1)\,|\,\Psi_\kappa\,|^2\ . \tag{5}$$

In all our examples the bound-electron charge distribution outside the ion sphere was negligibly small.

The free-electron spatial distribution is assumed to follow Fermi-Dirac statistics:

$$n_f(r,\mu)=\frac{1}{2\pi^2}\left[\frac{2mkT}{h^3}\right]^{3/2}F_{1/2}\left[\frac{\mu-eV(r)}{kT}\right]\ , \tag{6}$$

where

$$F_j(x)=\int_0^\infty\frac{y^j}{\exp(y-x)+1}dy\ , \tag{7}$$

and μ is the chemical potential, which is solved numerically from the equation

$$Z_f=\int_0^R n_f(r;\mu)d^3r\ . \tag{8}$$

The solutions for the densities $n_f(r)$ and $n_b(r)$ are then substituted back into Eq. (1) to yield a better approximation for the potential $V(r)$ and the whole procedure is repeated until convergence is attained. In this sense the final potential can be regarded as self-consistent in both the bound and free electrons. Exchange interactions are introduced through a zero-temperature Slater-type exchange potential,

$$eV_{\rm xc}(r)=-\frac{3e^2}{4\pi}[3\pi^2 n_e(r)]^{1/3}\ , \tag{9}$$

where $n_e(r)$ is the total (bound plus free) electron density.[13] For the calculations of the bound-electron wave functions a Latter-tail-type asymptotic behavior [for $r\to\infty$, $rV(r)\sim-(Z-Z_b-Z_f+1)=-1$] was used in calculating n_b, but not n_f (since the calculation is classical, not from wave functions). The Latter tail affects mainly the threshold behavior of the photoionization cross section, in fact, Cauble *et al.*[5] who did not include it in their calculation found a continuous-threshold behavior rather than an edge structure. At present, the physical significance of the Latter tail in hot and dense plasmas is still an open question and a separate research into this problem would be highly desirable.

Our calculation lacks a few ingredients, which were included in various previous works. First, the free-electron correlations[4,8,14] are neglected. These are introduced generally by means of an effective potential, but they probably have only minor effects on the results.[8] Second, no finite-radius boundary conditions are used,[2] thereby limiting our treatment to atomic states which are not too close to the ionization limit.[15] Finally, the neighboring ions' spatial distribution is implicitly included in the ISM by assuming a neutral background beyond the ion sphere, rather than using an explicit pair-correlation function[6] (radial distribution function[11]) $g(r)$. For very high coupling constants Γ such a description may be inadequate, as a lattice-type structure builds up in the plasma; but for $\Gamma\leqq 5$, which is the limit of our present calculations, a homogeneous-ion distribution beyond the ion sphere is still a plausible approximation.[6,11]

Similarly to the bound-state wave function, the continuum-state wave function of the outgoing photoionized electron was found by solving the Dirac equation in the same self-consistent field as the bound electron. These wave functions were used to compute single-particle bound-free transition matrix elements and photoionization cross sections which incorporate relativistic, retardation, and higher multipole effects.[16,17]

III. RESULTS

Calculations were carried out for a pure-aluminum plasma at $kT=500$ eV and ion densities of $n_T=10^{20}$, 10^{21}, 10^{22}, 10^{23}, and 3×10^{23} atoms/cm^3, corresponding to coupling constants of $\Gamma=0.31$, 0.67, 1.44, 3.1, and 4.5. For all these densities we considered the following species, which are the most abundant charge and ionic states in the given temperature and density ranges.

Al XIII (H-like): $1s,2s,2p,3s,3p,3d$.

Al XII (He-like): $1s^2,1s2s,1s2p,1s3s,1s3p,1s3d$.

Al XI (Li-like): $1s^22s,1s^22p,1s^23s,1s^23p,1s^23d$.

The upper limit for the computations of the photoionization cross sections was $h\nu\leqq 20$ keV, because no new interesting density-dependent phenomena were observed above this limit. As a lower limit we have chosen the M edge. The reason for this choice was not only the intent to save computation time, but also the fact that below this limit inverse bremsstrahlung rather than photoionization becomes the dominant photoabsorption process[7] in a hot and dense aluminum plasma.

In the present work we concentrated mainly on the influence of the density variation on the plasma properties. Nevertheless, we have checked the effects of temperature for a few cases under discussion. We have found that the main influence of an increased temperature is to produce a more homogeneous free-electron distribution but generally temperature variations had only minor effects on the binding energy relative to those produced by the density variations. The temperature, as well as density, behavior of the occupation numbers, was nonetheless explicitly inserted into our computations.

Three models are compared in the present paper.

(1) First, we carried out full DC-type computations for all the above ionic states. The occupation numbers used for this case were obtained from a full non-LTE-type steady-state calculation,[18] using the low-density values for the rate coefficients of the various atomic processes; this fact, however, does not reduce the accuracy of our results, because at the lower densities the rate coefficients are sufficiently close to their low-density limit, and at the higher densities, where LTE conditions are established, the occupation numbers are independent of the exact expressions used for the rate coefficients.[19]

(2) In a second set of calculations we used an AA model with the same non-LTE occupation numbers as for the DC calculations. The aim of this calculation was to study the consequences of the basic assumption of the AA model, namely, that a fictitious ion can replace the charge- and excitation-state distributions in a real plasma. We shall refer to this model as the non-LTE-AA model.

(3) Finally, we used the predictions of a Thomas-Fermi (TF) charge- and excited-state distribution in an AA model to study the difference in the results from such a statistical LTE-type distribution for the occupation numbers and the results from more complete non-LTE-type distributions. In the following we shall refer to this model as the TF-AA model. The occupation numbers, the number of electrons in the various subshells, as well as the number of bound electrons used in the calculations are listed in Table I.

In Fig. 1(a), we show the screening factor $S(r)=rV(r)/Z$ for a particular configuration of DC model: $1s^22p$. Within the DC model wave functions and then cross sections are calculated in such potentials. To obtain plasma properties we then average over cross sections reflecting the abundances of the various ionic species.

TABLE I. Occupation numbers of the ionic states vs the ion density for the three models compared in this paper: DC, non-LTE-AA, and TF-AA.

Model and ion state	Density	10^{20}	10^{21}	10^{22}	10^{23}	3×10^{23}
DC[a]	Al III, $1s$	0.314	0.43	0.375	0.151	0.195
	Al III, $2s$[b]	4.3(−5)[c]	5.5(−4)	3.8(−3)	8.5(−3)	2.7(−2)
	Al III, $2p$					
	Al III, $3s$[b]					
	Al III, $3p$	2.5(−5)	3.7(−4)	4.0(−3)	9.9(−3)	3.5(−2)
	Al III, $3d$					
	Al XII, $1s^2$	0.660	0.49	0.343	0.241	0.311
	Al XII, $1s\,2s$	1.06(−3)	1.305(−3)	4.27(−3)	1.098(−2)	9.88(−3)
	Al XII, $1s\,2p$	2.79(−3)	3.565(−3)	12.35(−3)	3.208(−2)	2.89(−2)
	Al XII, $1s\,3s$[b]					
	Al XII, $1s\,3p$	8.21(−4)	3.04(−3)	1.865(−2)	5.46(−2)	4.97(−2)
	Al XII, $1s\,3d$					
	Al XI, $1s^2 2s$	1.61(−3)	1.29(−3)	3.43(−3)	1.28(−2)	2.01(−2)
	Al XI, $1s^2 2p$	4.26(−3)	3.40(−3)	9.64(−3)	3.67(−2)	5.76(−2)
	Al XI, $1s^2 3s$	1.61(−4)	3.33(−4)	1.77(−3)	7.63(−3)	1.21(−2)
	Al XI, $1s^2 3p$	4.52(−4)	9.73(−4)	5.25(−3)	2.26(−2)	3.58(−2)
	Al XI, $1s^2 3d$	6.37(−4)	1.55(−3)	8.67(−3)	3.75(−2)	5.94(−2)
non-LTE-AA[d]	$n=1$	1.653	1.435	1.154	1.06	1.215
	$n=2$	9.8(−3)	8.8(−3)	3.3(−2)	7.0(−2)	0.233
	$n=3$	2.0(−3)	6.3(−3)	3.8(−2)	0.16	0.172
	Number of bound electrons	1.665	1.450	1.226	1.290	1.620
TF-AA[e]	$n=1$	0.189	0.385	0.702	1.26	1.62
	$n=2$	0.039	0.053	0.103	0.22	0.31
	$n=3$	0.046	0.067	0.120	0.18	0.23
	Number of bound electrons	0.274	0.505	0.925	1.66	2.16

[a]Numbers corresponding to the DC model are the partial densities relative to the total ion density (Ref. 18).
[b]Distributed on the subshells statistically.
[c]4.3(−5) means 4.3×10^{-5}, etc.
[d]Numbers corresponding to the non-LTE-AA model represent the number of bound electrons per ion in the given shell. These numbers are obtained, in fact, by averaging the DC model results, see main text.
[e]Number of bound electrons for the TF-AA model was obtained from a parametrization of the TF model (see Ref. 4) and were distributed according to a Boltzmann-type distribution among the various excited states. Numbers for this case, like for the non-LTE-AA case, represent the number of bound electrons per ion in the given shell.

These versions of $S(r)$ are shown in Fig. 1, obtained by treating the exchange term in three different ways: (1) a Slater-type exchange potential (curve 1), leading to a discontinuity at the ion-sphere radius due to the finite continuum charge density at that point, (2) without any exchange term (curve 2), and (3) a Slater-type exchange term, with a transition to no exchange in the region near the ion-sphere radius (curve 3). It was found that the differences in inner-shell binding energies or wave functions between type-1 and type-3 potentials are negligibly small, and the resulting difference in inner-shell photoionization cross sections mainly occurs near threshold, with a variation of 10% or less (except for some threshold oscillations). For the convenience of calculation, we have used type-1 potentials in this work. [The results from type-1 and type-2 potentials are much more different, illustrating that the variation in potential at small distances ($\sim10^{-2}$—10^{-1} a.u.) has important effects on the photoionization cross section. This is also the reason we show the screening factor in a logarithmic scale in Fig. 1.]

Figures 1(b) and 1(c) show the behavior of the screening factor $S(r)=rV(r)/Z$ for a relatively low-density plasma of 10^{20} ions/cm^3 [Fig. 1(b)] and for the high-density case of 10^{23} ions/cm^3 [Fig. 1(c)] for the three models which are the subject of the comparison in the present paper. Here (as in some future figures) the DC model might have been averaged over an appropriately weighted configuration. The screening factor is a monotonically decreasing function of the radius; the decrease is significantly sharper for the higher-density case due to the stronger screening of

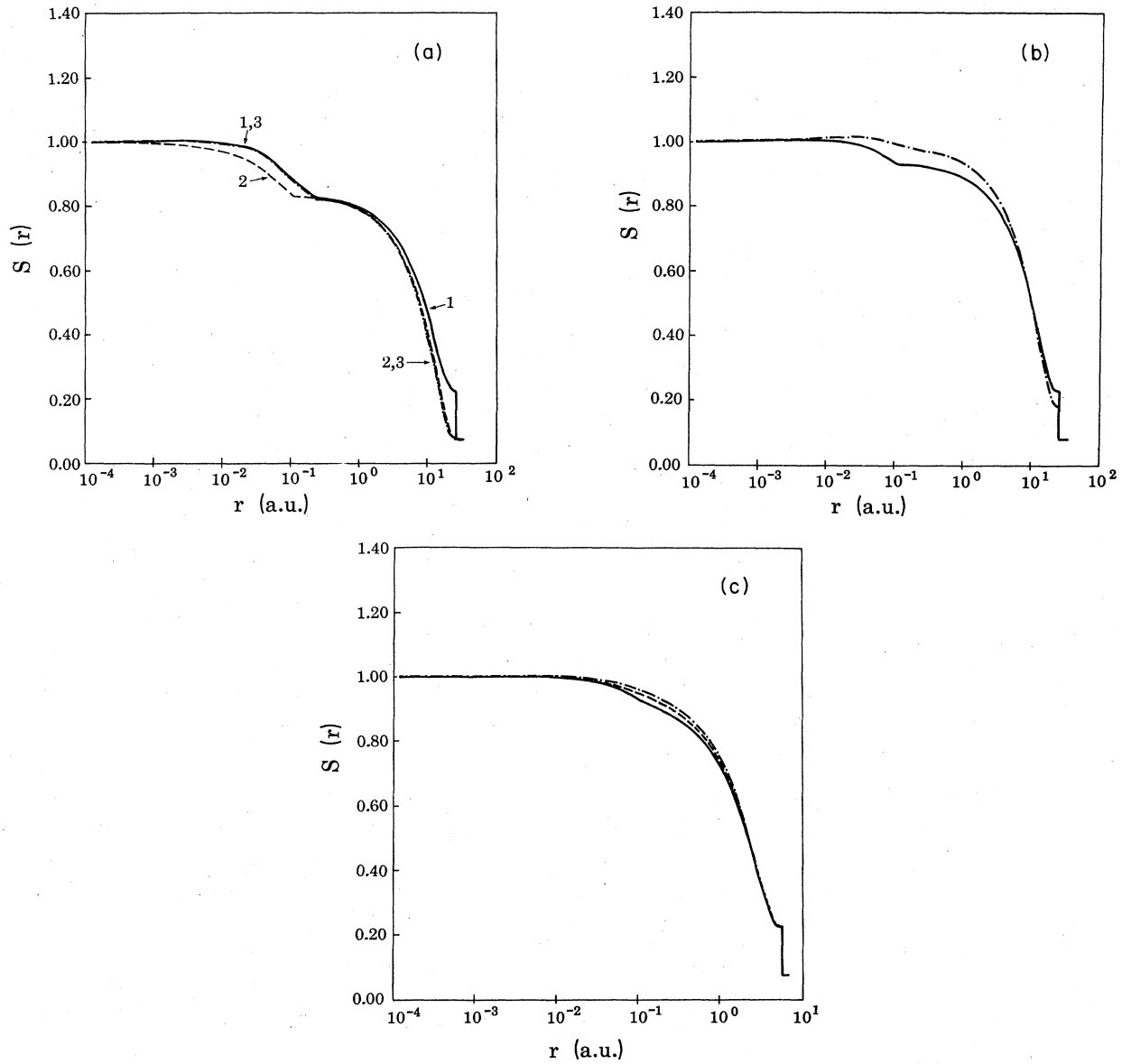

FIG. 1. (a) Comparison of the screening factors $S(r)=rV(r)/Z$: (1) with full exchange term, (2) without exchange term, and (3) with exchange only in the interior of the ion volume. Case shown is for the ground state of a H-like ion, in the DC model, at ion density 10^{20} cm^{-3} and temperature $T=500$ eV. (b) Screening factors for the DC model averaged over the relevant configurations (solid line) and TF-AA model (dash-dotted line). Non-LTE-AA result essentially overlaps TF-AA. Density is 10^{20} cm^{-3}, $T=500$ eV. (c) Same as (b), but ion density is 10^{23} cm^{-3}.

the free electrons. The distance at which the screening factor is reduced to $S(r)=0.5$ is roughly proportional to the ion radius. The effect of bound-electron screening in the low-density case can be observed as a sharp change in the slope of $S(r)$ near the radius of the bound-electron orbital (~ 0.1 a.u.). In the high-ion-density case [Fig. 1(c)] this change in the slope is smoother due to the higher influence of the free-electron screening on the potential. A comparison between the various models in the low-density case reveals that the difference between the screening factors as calculated by the DC and non-LTE-AA models is very small, whereas the TF-AA model exhibits a somewhat different behavior due to the different distribution of the total electron charge between bound and free electrons. In fact, the TF-AA model predicts a smaller number of bound electrons, a correspondingly reduced charge polarization around the nucleus and, therefore, a smoother screening factor at small distances [see Figure 1(b)]. In the high-density case [Fig. 1(c)] the three models predict a similar division of the electrons between bound and free, leading to the very small difference in the screening factors calculated in the three models.

The variation with ion density of the free-electron spatial distribution in the ion sphere of a ground-state H-like ion, in the DC model, is shown in Fig. 2. A sharp increase in the free-electron density occurs near the nucleus,

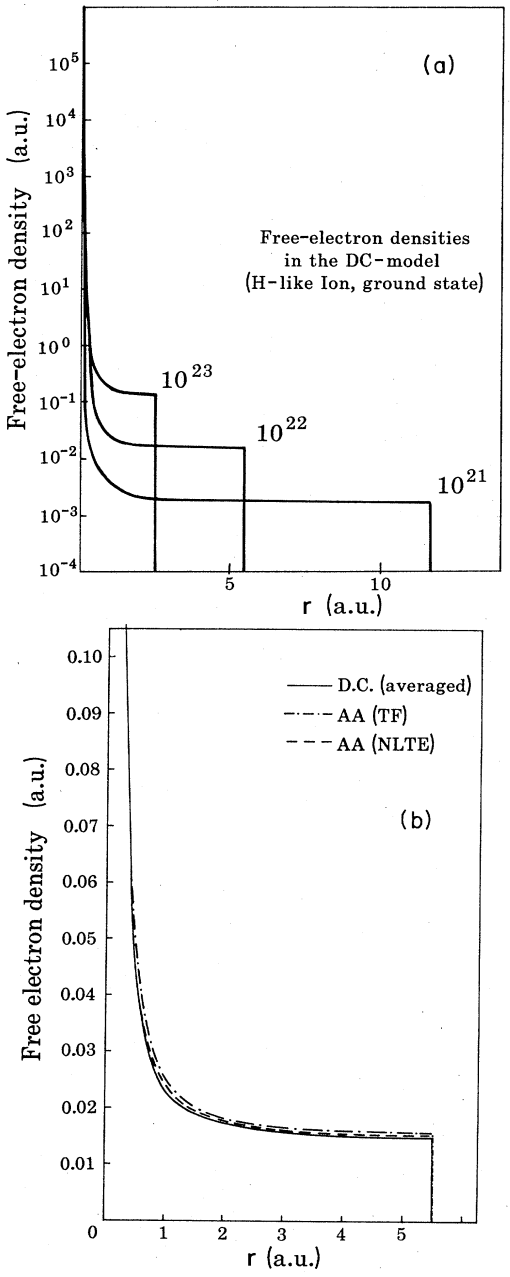

FIG. 2. Variation of the free-electron spatial distribution surrounding a ground-state hydrogenlike ion, (a) for various total ion densities in the DC model and (b) a comparison between the various models for ion density of 10^{22} cm^{-3}.

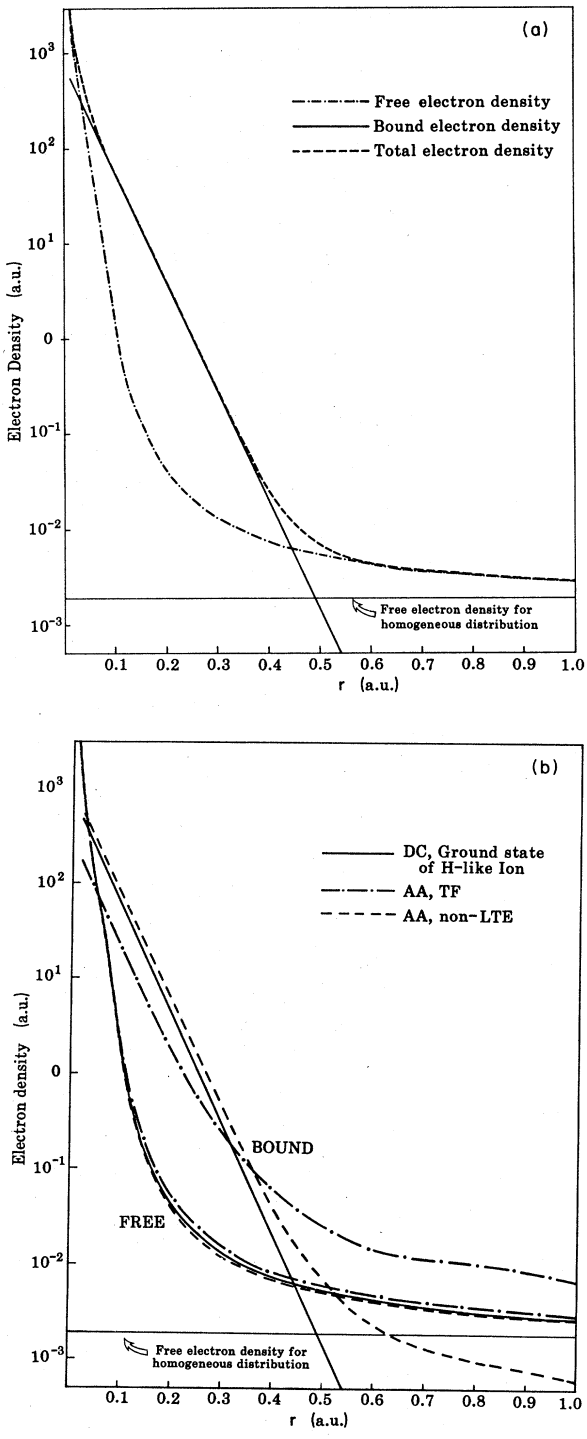

FIG. 3. (a) Bound (solid line), free (dash-dotted line), and total electron (dashed line) charge distributions for the DC model in the case of a ground-state hydrogenlike ion with ion density of 10^{21} cm^{-3}, $T=500$ eV. (b) Distributions of the free and bound electrons for a ground-state H-like ion in the DC (solid line), non-LTE-AA (dashed line), and TF-AA models (dash-dotted line) at the density 10^{21} cm^{-3} and temperature $T=500$ eV.

while the distribution is almost uniform at larger distances. It can be shown that for a Fermi-Dirac distribution the transition between these two regions occurs around $r \approx Za_0/(-\mu)$. Close to the nucleus the free-electron distribution is practically independent of the plasma density. This behavior is a consequence of Eq. (6), whose asymptotic behavior near the nucleus where

$eV(r) \gg |\mu|$, is $F_{1/2}(eV(r)/kT) \rightarrow \frac{2}{3}[eV(r)/kT]^{3/2}$, which is independent of the plasma density. In spite of the very high density, the total number of electrons in the high-density region, however, is very small because of its tiny dimensions. The use of Eq. (9), assures that the free-electron distribution is largely independent of the model used for the computation and the difference between the predictions of the three models was insignificant.

In Fig. 3 the details of the free- and bound-electron distributions near the nucleus are shown together with a comparison of these distributions in the various models. It can be seen that for a density of $n_T = 10^{21}$ cm^{-3} the free-electron density at the average radius of the $1s$ orbital (~ 0.10 a.u.) is more than 1 order of magnitude smaller than the bound-electron density, greatly reducing the free-electron influence on the $1s$ electron wave function at this density. At higher densities this influence is increased and becomes important.

In Fig. 4(a) the large component of the $3p_{1/2}$ wave function in an excited lithiumlike aluminum ion ($1s^2 3p$) is plotted for ion densities of $n_T = 10^{20}$ and 10^{23} cm^{-3} as calculated within the framework of the DC model. As a consequence of the higher free-electron screening in the higher-density plasmas, the bound-electron wave function is significantly shifted away from the nucleus. This results in a reduced binding energy. In Fig. 4(b) the same DC wave function is compared with the $3p_{1/2}$ electron wave functions in the two AA models, for a density of 10^{23} cm^{-3}. As mentioned earlier, at such a high density the level populations of the two AA models are rather close to each other (and to an LTE Boltzmann-type distribution), both having slightly more than one electron in the K shell, 0.1—0.2 electrons in the L shell and about 0.16—0.18 electrons in the M shell. The resulting wave functions in the two AA models are therefore rather similar. (But as the number of bound electrons is less in these two AA models than in the DC case, the $3p_{1/2}$ electron is farther away from the nucleus in a DC model due to the stronger screening by the larger number of $1s$ bound electrons, even though there is weaker free-electron screening.)

The variation of the $1s$ and $2p$ electron binding energies in hydrogenlike and heliumlike ions versus density is shown in Figs. 5(a) and 5(b), together with the corresponding variation for a plasma having a homogeneous free-electron distribution.[8,12] The binding energies follow the values obtained from a homogeneous distribution up to $n_T \cong 10^{22}$ cm^{-3}. Substantial deviations from this form can be observed only above this density, reflecting the importance of the nonhomogeneous free-electron distributions in high-density plasma. The corresponding variations in the AA models and their comparison to the average binding energy in the DC model are shown in Fig. 5(c). It is interesting to note that at low density the binding energy of the non-LTE-AA model tends to the average binding energy of the DC-model, but at high density they differ significantly from each other. The TF-AA model deviates from both of them at low density but comes closer to them at higher densities.

Examples of the photoionization cross sections versus photon energy from individual species are shown in Fig.

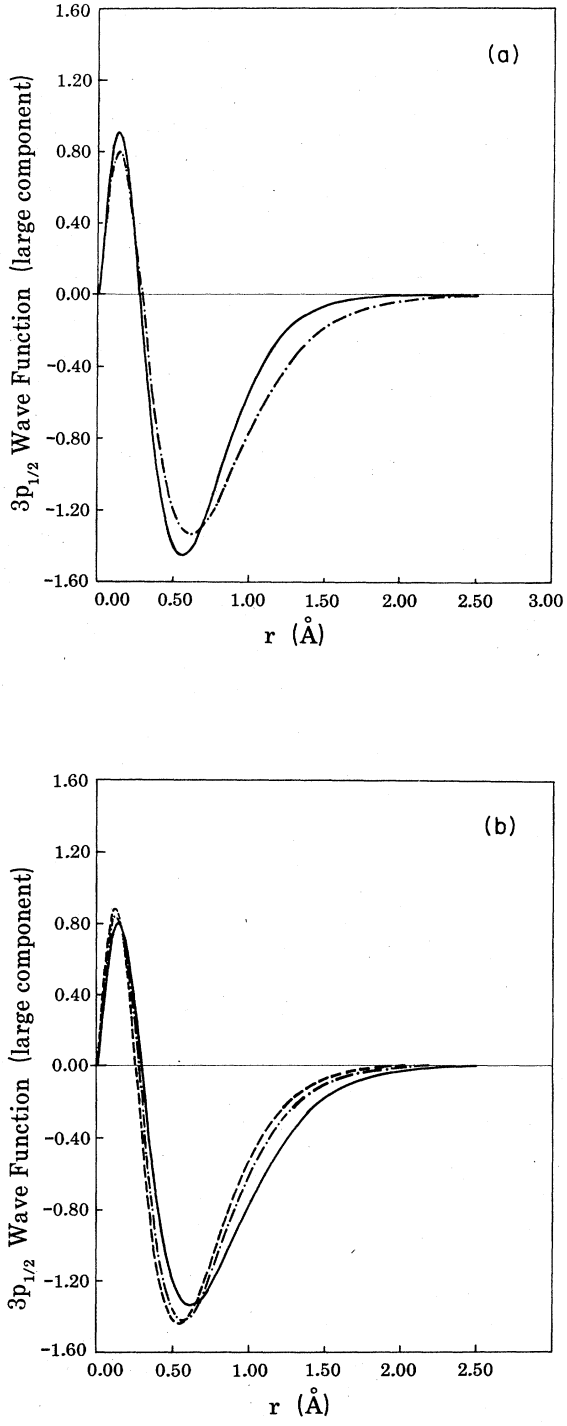

FIG. 4. (a) Comparison of the $3p_{1/2}$ wave function (large component) at densities of 10^{20} cm^{-3} (solid line) and 10^{23} cm^{-3} (dash-dotted line) for a $1s^2 3p$ excited lithiumlike ion as calculated in the DC model. $T = 500$ eV. (b) Comparison of the $3p_{1/2}$ wave functions of Li-like excited ions obtained by using DC model (solid line), non-LTE-AA model (dashed line) and TF-AA model (dash-dotted line) at density 10^{23} cm^{-3}. $T = 500$ eV.

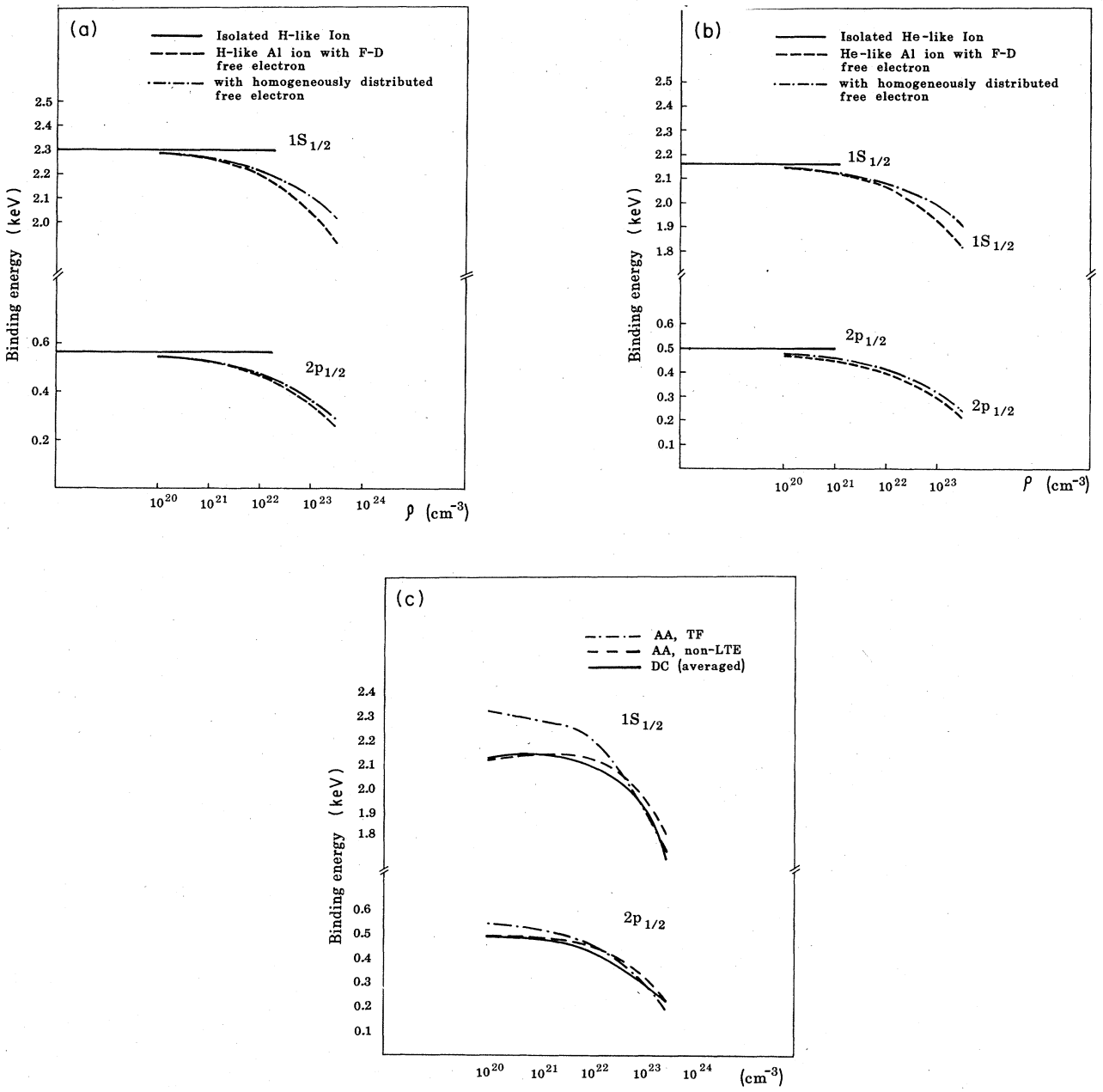

FIG. 5. Binding energies vs density of $1s_{1/2}$ and $2p_{1/2}$ electrons in a special configuration of DC model, (a) hydrogenlike and (b) heliumlike aluminum ions (dashed lines), with a Fermi-Dirac (FD) type of free-electron distribution. Horizontal solid lines denote the corresponding binding energies of an isolated ion. Binding energies for a homogeneous free-electron spatial distribution are also shown (dash-dotted line). In (c) a comparison is shown between the average binding energy in the DC model (solid line) and those obtained from the two AA models (non-LTE-AA, dashed line; TF-AA, dash-dotted line). $T=500$ eV.

6, for $1s$—continuum transitions in hydrogenlike ions. It can be seen that in the high-photon-energy portion of the photoionization cross section there are only minor variations (of the order of a few percent) with density. The reason for this behavior is that the greatest contribution to the cross section in this portion of the spectrum comes from photon-electron interactions close to the nucleus. Due to the small dimensions of this interaction volume the free-electron screening effects are negligibly small. Near threshold, however, there are significant differences with density, originating from the larger interaction volume. These differences appear both in the location of the absorption edge and the behavior of the cross section. Unfortunately, the ion-sphere model is not accurate

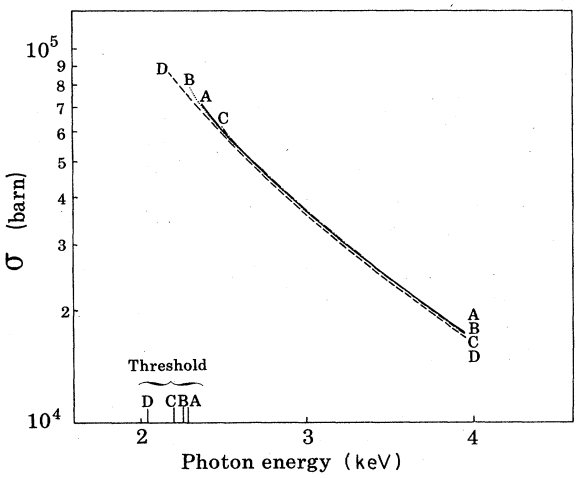

FIG. 6. Photoionization cross sections of a hydrogenlike ion, DC model, vs photon energy at the densities of *A*, 10^{20} cm^{-3}; *B*, 10^{21} cm^{-3}; *C*, 10^{22} cm^{-3}; *D*, 10^{23} cm^{-3}; for $1s \rightarrow$continuum. $T = 500$ eV.

enough close to the ion-sphere boundary and cannot, therefore, be used for an accurate quantitative study of the threshold region of the photoionization cross section. In principle, at very high densities the self-consistent potential should greatly differ from a Coulomb potential and, consequently, one would expect non-Coulomb phenomena in the behavior of the cross sections, such as the appearance of Cooper minima, delayed maxima or shape resonances. The role of these important phenomena in hot and dense plasmas requires separate investigation.

Our final results are concentrated in Figs. 7 and 8. In Fig. 7 we compare the photoionization cross sections as calculated by the DC and the non-LTE-AA methods. The following four features are noteworthy.

(i) The two models yield the same results for the high-energy portion (above the *K* edge) of the cross section. Only for very high densities, $n_T \geqq 10^{23}$ cm^{-3}, is there a 15—20% decrease of the DC model cross section relative to the AA results. This behavior, already mentioned in context of Fig. 6, stems from the fact that the main contribution to this portion of the spectrum comes from a small interaction volume near the nucleus, and the difference between the models is measurable only at high densities when the distortion of the potential due to the presence of free electrons within this volume becomes significant.

(ii) The DC model calculations predict structured edge regions with the main edges split into several partial edges corresponding to the relevant charge states and excited states in the plasma. This is in contrast to the sharp single-edge structure from the AA model.

(iii) Curiously, the *L* and *M* edges, as calculated from the AA model are not in the average position of the *L* and *M* edges of the real plasma but somewhat higher than the maximum *L* or *M* position. This fact follows from an inherent difficulty of the AA model: The plasmas described in this paper, at all densities, contain mainly ground-state H-like ions (see Table I), with only a very small percentage of $n = 2$ or 3 excited states. The greater number of the *L* and *M* electrons in the plasma populate the ground- and excited-state lithiumlike or excited heliumlike ions. Nevertheless, the averaging procedure of the AA model provides an atom with about one *K* electron, namely an "almost" hydrogenlike atom, with a very small number of *L* and *M* electrons. Naturally, these electrons will realize a potential which is close to the potentials felt by excited electrons in heliumlike ions, and not the average of the potentials as used in the DC model, resulting in edges close to the excited heliumlike *L* or *M* edge. The AA model, therefore, cannot reproduce correctly photoionization in the edge region and it has a broader dip region below threshold than the DC model.

(iv) The previous remarks have one more consequence: since the *L* edge in the DC model is split into several edges, the lowest of which is significantly below the *L* edge of the AA model, the ratio of edge tip-to-dip is much smaller in the DC model than is predicted by the AA model. In fact, at high densities, above $n_T \sim 10^{22}$ cm^{-3}, the DC model predicts a dip that is so shallow that the cross section can be regarded as almost continuous in the *L*-edge region (and probably also for lower edges).

In Fig. 8 a comparison between the non-LTE-AA model and the TF-AA models is shown. In this comparison we studied the influence of using LTE population numbers in an AA-type calculation versus more accurate non-LTE occupation numbers in the same model. Large quantitative differences can be observed between the results of the two models. At low densities, $n_T = 10^{20}$ cm^{-3}, the two cross sections differ by a factor of 5 in the regions of the *K* and *L* slopes, by a factor of 20 near the *L* edge, and up to 3 orders of magnitude near the *K* edge (including the effect of the edge shift). As the density increases, the non-LTE-AA model population approaches the LTE-type distribution and as expected the curves become closer to each other.

In the present paper we studied the difference between the predictions for the photoionization cross sections of the detailed configuration and the average-atom models in the framework of the ion-sphere self-consistent potential. We have found that when using the same occupation numbers in these two models, substantial differences are observed near the absorption edges and in the low-photon-energy portion of the spectrum, while smaller differences occur above the *K* edge. We have also found that the results are very sensitive to the occupation numbers used and inadequate accuracy in the population of the ionic states results in enhanced inaccuracies in the computed photoionization cross sections.

The relative importance of the accuracy of the predictions of the various models depends, in principle, on the spectrum emitted from the plasma. For a continuous emission spectrum the increase of the radiation reabsorption in a DC-type calculation relative to an AA-type calculation is of the order of the ratio of the edge shift between the results of the two computations to the energy difference between two neighboring edges $(\Delta h\nu)_{\text{DC-AA}}:(\Delta h\nu)_{\text{edge}}$. This estimate gives an increase of 9% near the *K* edge and 38% near the *L* edge of the opa-

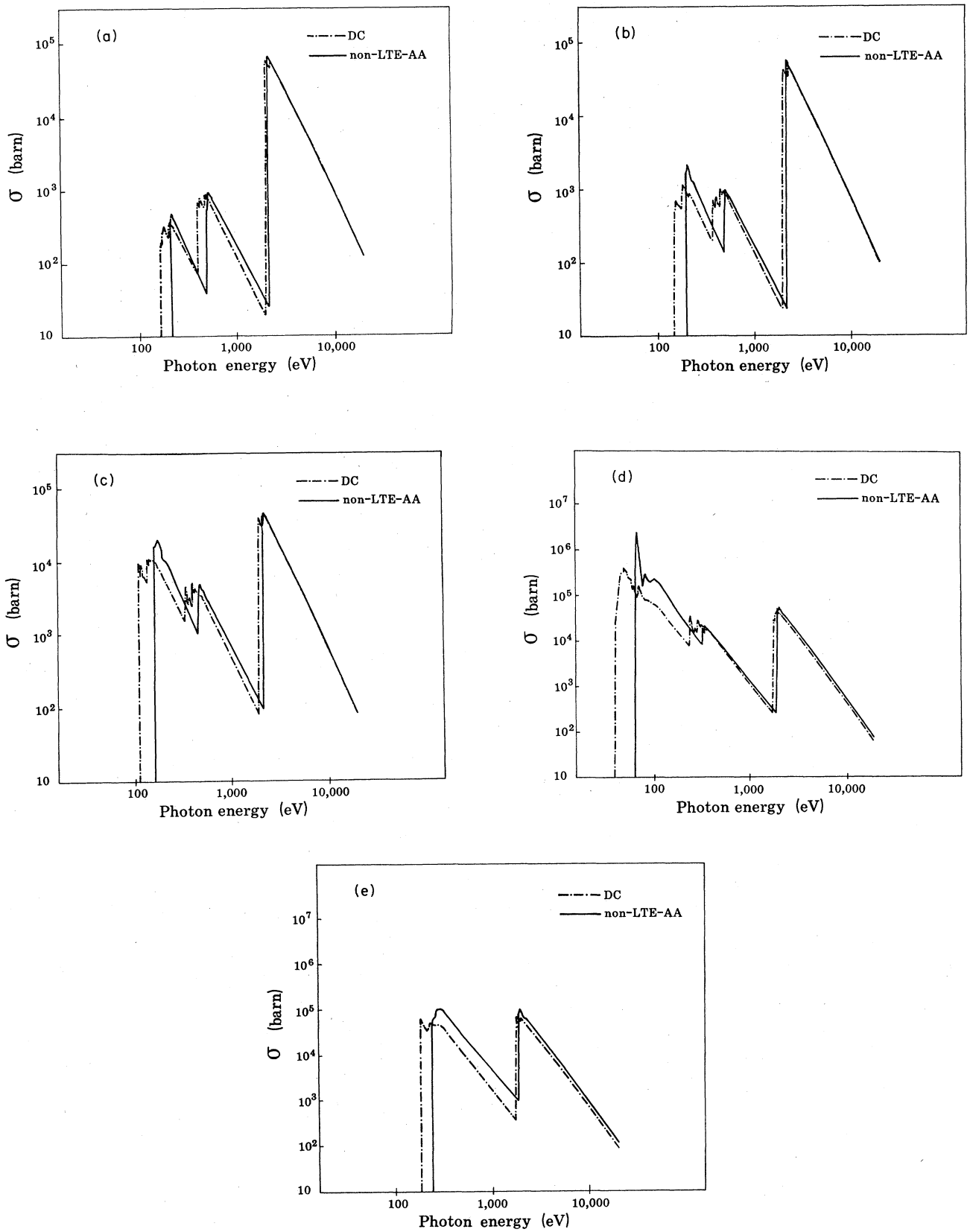

FIG. 7. Comparisons of the photoionization cross sections as calculated by DC and non-LTE-AA models at densities of (a) 10^{20} cm^{-3}, (b) 10^{21} cm^{-3}, (c) 10^{22} cm^{-3}, (d) 10^{23} cm^{-3}, and (e) 3×10^{23} cm^{-3} (without M shell cross sections). $T=500$ eV.

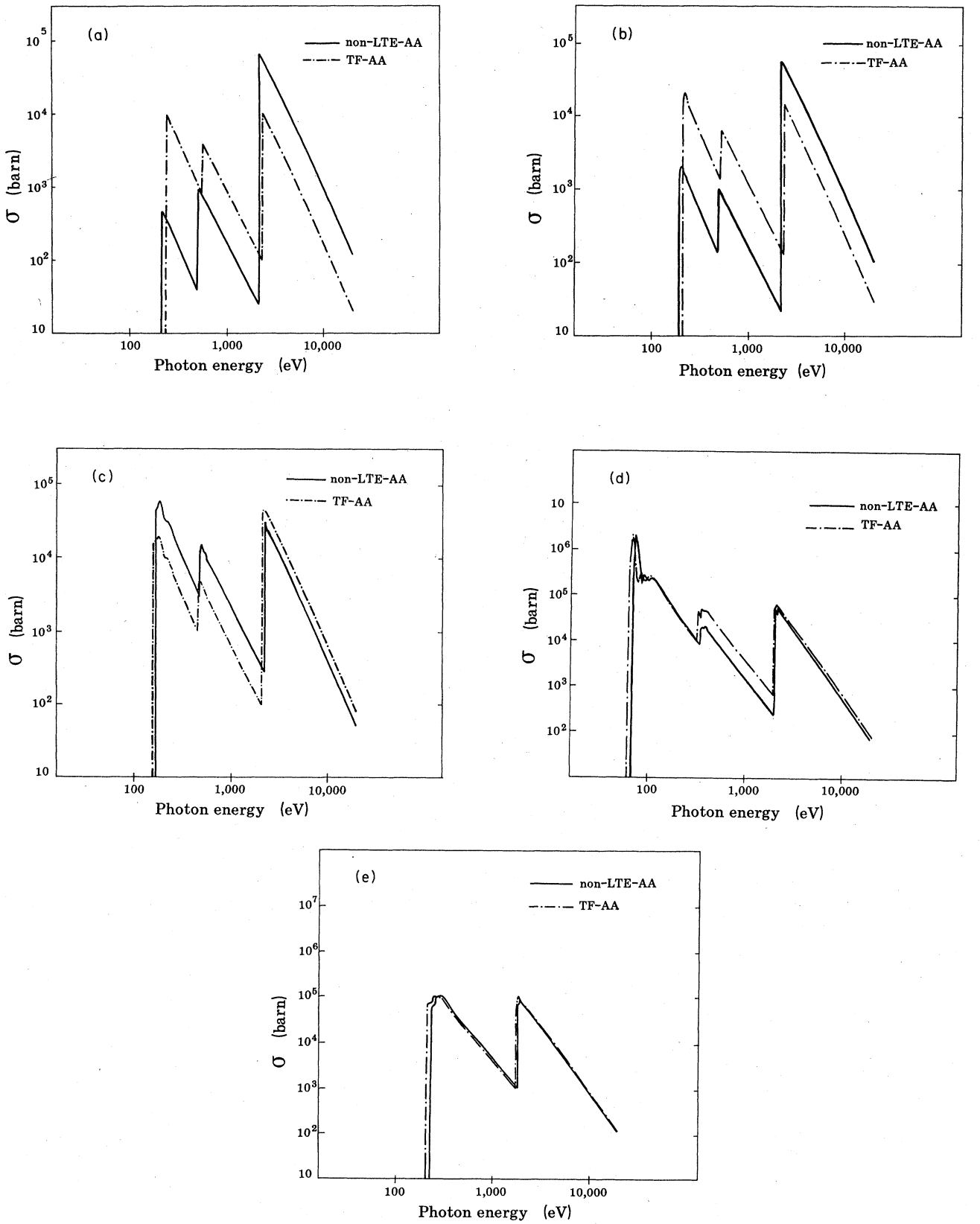

FIG. 8. Comparison of the photoionization cross sections calculated by non-LTE-AA and TF-AA models at densities of (a) 10^{20} cm^{-3}, (b) 10^{21} cm^{-3}, (c) 10^{22} cm^{-3}, (d) 10^{23} cm^{-3}, and (e) 3×10^{23} cm^{-3} (without M shell cross sections). $T=500$ eV.

city at a density of 10^{20} atoms/cm^3. These numbers grow, respectively, to 12% and 45% at a density of 10^{23} cm^{-3}.

The situation becomes significantly more complicated for the realistic case when the spectrum is emitted from an aluminum plasma in temperature and density conditions similar to the absorbing plasma, such as in laser-produced plasmas. In this case, the reabsorption of the line spectrum by resonant line absorption should also be accounted for. Since both the line emission and the resonant photoabsorption appear right below the edges, their combined effect may reduce the relative importance of the photoionization in this spectral region and, consequently, also the importance of the differences in the results of its computation in the various schemes. This turns out to be true, however, only at relatively low densities (10^{20} cm^{-3}). At high-density plasma ($\sim 10^{23}$ cm^{-3}) the highly excited states ($n \geq 4$) merge into the continuum so that the emitted line spectrum as well as the corresponding line photoabsorption are greatly thinned out and broadened, and the photoionization process regains its relative importance also in the spectral region below the edges, particularly the lower edges. All in all, one would expect that the effect of the differences between the DC and AA methods of computation will be significant for high-density plasmas especially right below the low-energy absorption edges. This conclusion will generally hold true for other elements also.

The photoionization cross section is the dominant photoabsorption effect in the 0.1—100-keV region.[7] Other important photoabsorption processes are the following:[7] (i) the resonant (bound-bound) line absorption is dominant below the absorption edges; (ii) inverse bremsstrahlung is the principal absorption process at low energies, below ~ 100 eV; (iii) the Compton effect prevails above a few tens of keV's; and, finally, (iv) pair production is effective above $2mc^2$. All these processes are density dependent, and for a complete computation of the total photoabsorption cross section in high-density plasmas an investigation of their density dependence would also be needed.

ACKNOWLEDGMENTS

The authors would like to thank Dr. Dwight Duston of the Naval Research Laboratory for providing his results for the non-LTE occupation numbers used in the present work. One of the authors (R.Y.Y.) also wishes to acknowledge financial support from the Andrew-Mellon Foundation.

---

*On sabbatical leave from Soreq Nuclear Research Center, Yavneh 70600, Israel.

[1]J. N. Bahcall, W. F. Huebner, S. H. Lubow, P. D. Parker, and R. G. Ulrich, Rev. Mod. Phys. **54**, 767 (1982).

[2]B. F. Rozsnyai, Phys. Rev. A **5**, 1137 (1972).

[3]B. F. Rozsnyai, J. Quant. Spectrosc. Radiat. Transfer **27**, 211 (1982).

[4]R. M. More, Lawrence Livermore Laboratory Report No. UCRL-84991, 1981 (unpublished).

[5]R. Cauble, M. Blaha, and J. Davis, Phys. Rev. A **29**, 3280 (1984).

[6]M. W. C. Dharma-Wardana and F. Perrot, Phys. Rev. A **26**, 2096 (1982).

[7]D. Salzmann and G. Wendin, Phys. Rev. A **18**, 2695 (1978).

[8]S. Skupsky, Phys. Rev. A **21**, 1316 (1980).

[9]J. Davis and M. Blaha, J. Quant. Spectrosc. Radiat. Transfer **27**, 307 (1982).

[10]D, A. Liberman, Phys. Rev. A **20**, 4981 (1979).

[11]S. Ichimaru, Rev. Mod. Phys. **54**, 1017 (1982).

[12]J. C. Stewart and K. D. Pyatt, Astrophys. J. **144**, 1203 (1966).

[13]A straightforward application of this formula introduces an unphysical discontinuity into the potential on the boundary of the ion sphere, originating from the discontinuity of the free-electron density. To check for the effect of this discontinuity on our results we repeated our calculations with an external smoothing procedure for the potential near the boundary region. Only close to the threshold did deviations show up between the two calculational methods.

[14]M. W. C. Dharma-Wardana and R. Taylor, J. Phys. C **14**, 629 (1981).

[15]It was suggested by Rozsnyai (Ref. 2) that the effect of such boundary conditions is to broaden the upper energy levels into an energy band, with increasing broadening for the states closer to the ionization limit.

[16]I. B. Goldberg, University of Pittsburgh Internal Report No. PITT-291, 1982 (unpublished).

[17]R. H. Pratt, A. Ron, and H. K. Tseng, Rev. Mod. Phys. **45**, 273 (1973).

[18]D. Duston and J. Davis, Phys. Rev. A **21**, 1664 (1980); **23**, 2602 (1981).

[19]D. Salzmann and A. Krumbein, J. Appl. Phys. **49**, 3229 (1978).